Investigation of the Source Space of Electrocardiography and Magnetocardiography using Isotropic and Anisotropic Thorax Models

M Nalbach, O Skipa, FB Sachse, O Dössel

Institute of Biomedical Engineering, Universität Karlsruhe (TH), Germany

Abstract

Noninvasive Imaging of the bioelectric processes on the heart using Electrocardiography (ECG) and Magnetocardiography (MCG) data is a widely discussed research topic of the recent years. The source space of ECG is compared with the source space of MCG and vice versa to investigate the difference of information content of these mapping techniques for source imaging purposes. The approach allows the calculation of the intersection and non-intersection part (the calculation of silent sources) of MCG (ECG) in comparison to ECG (MCG). The investigation was carried out on a Finite Element model which was constructed from a magnetic resonance imaging (MRI) dataset of a volunteer. Anisotropic fibre orientation was applied to myocardium to investigate its effect on the differences of the source spaces.

1. Introduction

Source reconstruction / source imaging is a promising tool in cardiac disease diagnostics using non-invasive mapping techniques like Body-Surface-Potential-Mapping (BSPM) and Magnetic-Field-Mapping (MFM). Which measurement data deliver more information for purposes of source imaging is discussed heterogeneously. The magnetic field of a radial currents vanishes in a spherical model whereas radial and tangential components can be detected by electric sensors. A closed current loop vanishes electrically but yields a magnetic signal. The curved shape of a curved current can only be acquired by magnetic sensors, electric measurements show a straight line current. This differences of the "information content" are known for simple geometries and simple source models. The determination of differences in the detectable information for complex models like an inhomogeneous, isotropic/anisotropic thorax model and distributed source spaces are determined in this simulation study.

2. Method

The model was constructed of a magnetic resonance imaging (MRI) dataset of a 28 year old volunteer which was recorded at the Institute of Biomedical Engineering,

ETH and University Zurich. This dataset was segmented using interactive deformable contours and region growing. Skin, skeletal muscles, fat, lungs, liver, kidneys, atria, ventricles and blood (in the heart) were classified. Fibre orientation was introduced in the ventricles to derive anisotropic conductivity using a rule-based approach [1]. The anisotropy ratio of conductivity was set in the physiological range 1:3.

Figure 1. Fibre orientation in the myocardium and source space of 288 distributed current dipoles.

The source space $\mathbf{x}$ is spanned by 288 distributed current dipoles (DCD) within the ventricles (Fig. 1: x,y,z-triplets in 96 locations). The electric and magnetic forward calculations were carried out using Finite Element Method (FEM) to take the anisotropic conductivity of the myocardium into account. The model was meshed into tetrahedron mesh consisting of 70000 nodes (Fig. 1). We calculate the transfer matrix (lead field matrix) $\mathbf{A}$ as a linear operator which transfers the source vector $\mathbf{x}$ to the measurement vector $\mathbf{b}$.

$$\mathbf{A} \mathbf{x} = \mathbf{b}$$

To improve the accuracy of the magnetic forward calculation the mesh was refined around each dipole location. An optimised point generator was used to refine the mesh for each dipole using more than 20000 nodes [2]. If all nodes were introduced simultaneously the model would consist of 6 million nodes which corresponds to about 42 million tetrahedrons. So, a separate model for each dipole including mesh refinement for the corresponding dipole was constructed, forward calculations were carried out and the refined points were erased for the next forward calculation to reduce memory and computational requirements (Fig. 2).
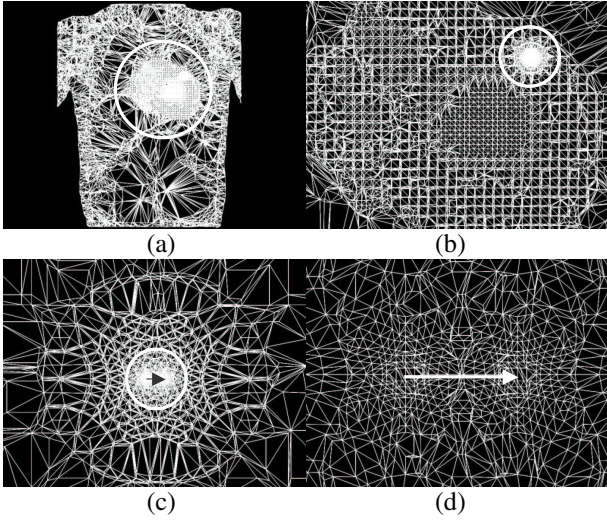
Figure 2. Adaptive mesh refinement for current dipole.

A singular value decomposition (SVD) approach is used for the reconstruction of the source vector $\mathbf{x}$ form the measurement data $\mathbf{b}$.

$$\mathbf{A} = \mathbf{U} \, \mathbf{S} \, \mathbf{V}^T$$
$$\mathbf{U} = \{\mathbf{u_i}\}, \; \mathbf{S} = \text{diag}\{\sigma_i\}, \; \mathbf{V} = \{\mathbf{v_i}\}$$
$$\mathbf{A}^{*-1} = \mathbf{V} \, \mathbf{R} \, \mathbf{S}^{-1} \, \mathbf{U}^T$$

The SVD yields the orthonormal base of the measurement space $\mathbf{U}$, the orthonormal base of the source space $\mathbf{V}$ and the corresponding singular values σ_i which are the weights between the measurement base vectors $\mathbf{u_i}$ and the source base vectors $\mathbf{v_i}$. The matrix $\mathbf{R}$ serves as a regularization function in the reconstruction process.

For the comparison of the source space two lead field matrices $\mathbf{A_1}$ and $\mathbf{A_2}$ from different sensor systems are given. The SVD of $\mathbf{A_1}$ and $\mathbf{A_2}$ delivers the source bases $\mathbf{V_1}$ and $\mathbf{V_2}$. The "main" subspace $\mathbf{V_{1m}}$ ($\mathbf{V_{2m}}$) of $\mathbf{V_1}$ ($\mathbf{V_2}$) is determined [3]. $\mathbf{V_2}$ ($\mathbf{V_1}$) is projected in the subspace $\mathbf{V_{1m}}$ ($\mathbf{V_{2m}}$) by the orthogonal projection $\mathbf{P_{1m}}$ ($\mathbf{P_{2m}}$). $\mathbf{V^{1m}_2}$ ($\mathbf{V^{2m}_1}$) is the part of $\mathbf{V_2}$ ($\mathbf{V_1}$) that is totally represented by the subspace of $\mathbf{V_{1m}}$ ($\mathbf{V_{2m}}$). $\mathbf{V^{1m}_2}$ is projected in the original space $\mathbf{V_2}$ using $\mathbf{P_2}$ to determine the intersection and non-intersection part of $\mathbf{V_2}$ in comparison to $\mathbf{V_1}$.

$$\mathbf{V^{1m}_2} = \mathbf{P_{m1}} \, \mathbf{V_2}$$
$$\mathbf{V^{1m,2}_2} = \mathbf{P_2} \mathbf{V^{1m}_2} = \mathbf{P_2} \mathbf{P_{m1}} \mathbf{V_2}$$

The norm $\|\mathbf{v^{1m,2}_{2,i}}\|_2$ of the projected $\mathbf{V^{1m,2}_2}$ shows how $\mathbf{V_2}$ is represented by the detectable source subspace $\mathbf{V_{1m}}$ [2][4].

3. Electric and magnetic mapping systems

In the virtual electric and magnetic sensor systems the magnetometers are placed on a regular, rectangular curved grid in front of the patient (Fig. 3, GMag). The corresponding electrode positions were found by projecting the magnetometer position onto the body surface and placed on the nearest surface node (GEle).
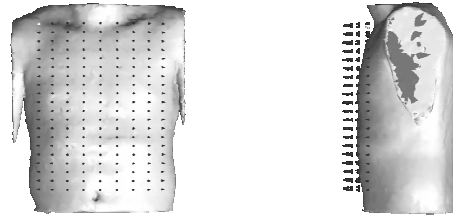

Figure 3. Magnetic device using 180 magnetometers (GMag).

We investigated a position optimised electrode arrangement versus a position optimised magnetometer system which were constructed by minimizing the slope of the singular values of the corresponding lead field matrix [3][4][5]. These systems are shown in Figure 4.
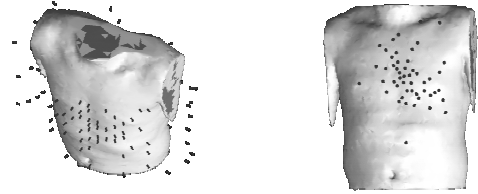

Figure 4. Optimised magnetic (OPTMag) and electric (OPTEle) sensor arrangements.

A real magnetic device, the Neuromag VectorView® system (BM99: 99 channel: 33 B_z-magnetometer, 33 dBz/dx-gradiometer, 33 dBz/dy-gradiometer) of the BioMag Laboratory, Helsinki University Central Hospital, Finland, and the 256–lead ECG (T256) of the Ragnar Granit Institute, Tampere University of Technology, Finland, were compared (Fig. 5). The device locations correspond to the positions of measurement circumstances during ECG and MCG studies of the given volunteer. The electrodes were digitised related to body landmarks (Polhemus Fastrak®). The magnetic sensor locations were determined using reference coils which were also digitised.
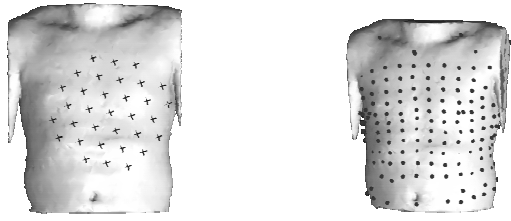
Figure 5. 99-channel MCG system of the BioMag Laboratory, Helsinki, and the 256-lead ECG of the Ragnar Granit Institute, Tampere.

4. Results

4.1. Norm of projected subspaces

The following graphs show the norm of the projected subspaces for the mapping arrangements of ECG in comparison to the MCG systems. Figure 6a, 7a, 8a shows results for isotropic conductivity in the myocardium and Figure 6b, 7b, 8b yields results for anisotropic conductivity.
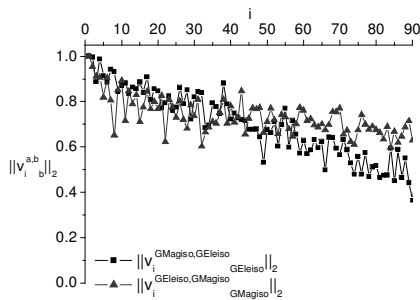

Figure 6a. Comparison of the projected source subspaces of GMag and GEle using isotropic conductivity in the myocardium.
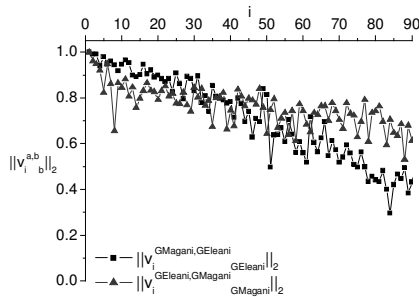

Figure 6b. Comparison of the projected source subspaces of GMag and GEle using anisotropic conductivity in the myocardium.

The comparison of the virtual magnetic grid device and the corresponding electrode arrangement features that there are source patterns especially in the source space of

MCG (index 8) up to an index of 50 which cannot be represented by the ECG subspace (Fig. 6a, 6b). The consideration of anisotropy yields an increasing of the projected ECG vectors that corresponds to a better representation by the MCG subspace.
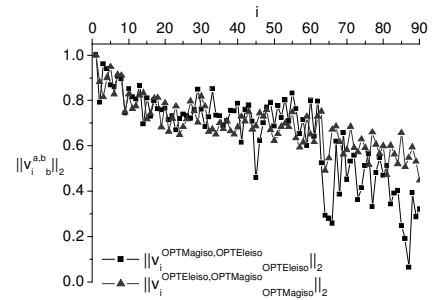

Figure 7a. Norm of the detectable source subspace of the optimised arrangements without fibre orientation.
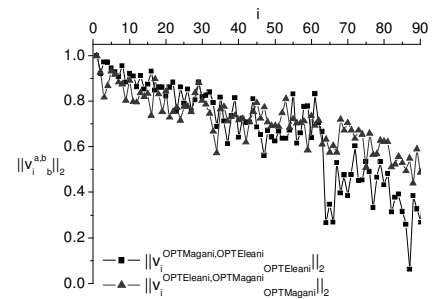

Figure 7b. Norm of the detectable source subspace of the optimised arrangements with fibre orientation.

The norms of projected source spaces of the optimised sensor geometries are shown in Figure 7a, 7b. In the isotropic volume conductor ECG and MCG shows differences in the first base vectors (index 2 for ECG and index 3 for MCG). There is a slight increase of the projected ECG space in anisotropic case as seen in the investigation of the grid devices ($\|v_2^{OPTMag,OPTEle}{}_{OPTEle}\|_2$ is increased).
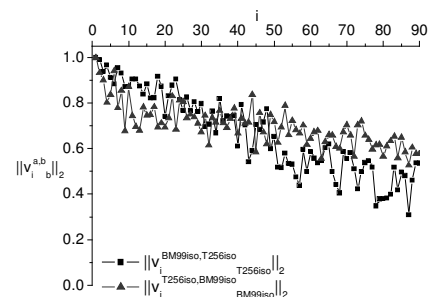

Figure 8a. Projected subspaces of MCG system BM99 and 256-lead ECG (T256) for isotropic heart model.
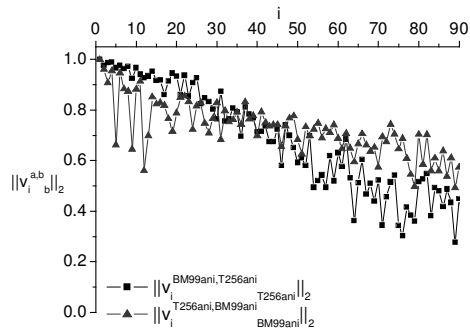
Figure 8b. Projected subspaces of BM99 and T256 for anisotropic heart model.

The comparison of real systems showed significant non-ECG-detectable source patterns especially for the anisotropic case, whereas the slope of the projected ECG vector norms is slightly lifted up (Fig. 8a, 8b).

Obviously, the projected subspaces depend significantly on the used sensor arrangement. The slopes of the norm of the projected subspace are quite similar for the optimised mapping systems and show strong ECG-silent patterns for the comparison of real measurement arrangements at low indices.

4.2. Electric silent sources

Figures 9, 10 show some source patterns which cannot be detected by the given ECG systems. There were identified by vectors which have low norm after projection.
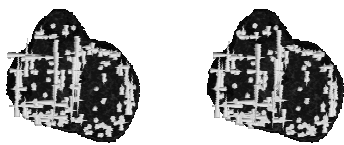

Figure 9. ECG silent source patterns of GMag and GEle (index 7: isotropic, anisotropic).

Figure 10. ECG silent source patterns of BM99 and T256 (index 5,9,12: anisotropic).

4.3. Magnetic silent sources

Examples of non-MCG-detectable patterns are shown in Figure 11.

It should be noted that strong MCG silent source patterns appear at higher indices.
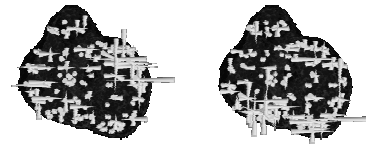

Figure 11. MCG silent source patterns of GMag and GEle (index 49: isotropic, index 51: anisotropic).

5. Conclusion and discussion

MCG and ECG show differences in the detectable source space. These differences (non detectable patterns) depend on the used measurement system (sensor geometry) and the anisotropy of conductivity of the myocardium. MCG yields theoretically more information than ECG if only MCG or ECG is used. Pathologies which can be expanded in „strong" ECG silent source patterns are not detectable by ECG. Anisotropy of conductivity of skeletal muscles and the influence of other modeling characteristics (more tissue classes, varying of conductivity and anisotropy ratios) were not investigated.

References

[1] Sachse FB, Frech R, Werner CD, Dössel O. A model based approach to assignment of myocardial fibre orientation. Computers in Cardiology, 1999;26:145-4.
[2] Nalbach M, Skipa O, Dössel O. The Source Space of Electrocardiography and Magnetocardiography. BioMag 2002;13:773-3.
[3] Schneider FR. Das inverse Problem der Elektro- und Magnetokardiographie. PhD thesis, Universität Karlsruhe (TH), Institut für Biomedizinische Technik, 1999.
[4] Nalbach M, Skipa O, Dössel O. Investigation of the source spaces of ECG electrode arrangements. Int J Bioelectromagnetism, 2002;2,4: 241-2.
[5] Nalbach M, Dössel O. Comparison of Sensor Arrangements of MCG and ECG with respect to information content. PhysicaC, 2002; 372-376:254-5.

Address for correspondence.

Marc Nalbach
Universität Karlsruhe (TH)
Institute of Biomedical Engineering
Kaiserstrasse 12
76128 Karlsruhe
Germany
Email: Marc.Nalbach@ibt.uni-karlsruhe.de
Web: www-ibt.uni-karlsruhe.de